U–Pb zircon age of the Hanano-yama pluton related to the mineralization in the Naganobori mine, Yamaguchi Prefecture, Japan

Teruyoshi Imaoka[1)*], Yasutaka Hayasaka[2)], Mariko Nagashima[1)], Takafumi Sonehara[3)] and Mana Miyauchi[4)]

Abstract The Naganobori mine was exploited for Cu from the late 7th to the early 8th centuries, helped to advance the ancient mining and manufacturing industries in the area around the Akiyoshi Plateau, Yamaguchi Prefecture, Japan, and is famous for producing the Cu used in national projects, such as minting the first coins in Japan (*Wadōkaichin and kōchō jūnisen*) and casting the Great Buddha of the Todaiji Temple. The relationship between the magmatism of the Cretaceous Hanano-yama plutons and mineralization in the Naganobori mine is investigated through field observations, petrography and U–Pb geochronology. The Hanano-yama granite porphyry, with a surface area of 0.8 km × 0.3 km, intruded the Paleozoic accretionary complex of the Akiyoshi Limestone in the eastern part of the Akiyoshi Plateau. Chemical analysis of rock-forming minerals revealed the existence of F-bearing minerals such as F-bearing biotite (max. 0.58 wt. %, ave. 0.41 wt.% F), titanite (4.42, 2.63 wt.%), fluorapatite (4.11, 2.96 wt.%), monazite-(Ce) (0.67, 0.58 wt.%), allanite-(Ce) (0.40, 0.18 wt.%). REEs are also enriched in titanite, fluorapatite, monazite-(Ce) and allanite-(Ce). This suggests that the fluorine and REE were significantly enriched in the residual melt and fluids after the crystallization of the Hanano-yama pluton. The U–Pb zircon age of the Hanano-yama pluton is 101.5 ± 0.7 Ma, which are identical to the Ofuku pluton with K–Ar hornblende and biotite ages of 97–101 Ma. From these age data, the Naganobori mine associated with Hanano-yama pluton belongs to the Tungsten Province of the San-yo Belt in Yamaguchi Prefecture, SW Japan, which is genetically related to the ilmenite-series granitoids.

Keywords: Hanano-yama granite porphyry, Naganobori mine, Cu mineralization, U–Pb geochronology, Tungsten Province

1. Introduction

Many mines in eastern part of the Akiyoshi Plateau, located in the central Yamaguchi Prefecture in SW Japan, were exploited for Cu from the late 7th to the early 8th centuries, advancing the ancient mining and manufacturing industries in the area around the plateau. In particular, the Naganobori mine (Fig. 1) is the oldest recorded one in Japan, and is famous for producing the Cu used in national projects, such as minting the first coins in Japan (*Wadōkaichin and kōchō jūnisen*) and casting the Great Buddha of the Todaiji Temple (Ikeda, 2004, 2015; Kuno, 1990; Saito, 2001a; Takahashi, 2001a; Yoshikawa *et al.*, 2005; Yoshimura *et al.*, 2014). The Naganobori mine is also the most likely source of Pb for the ancient Japanese Pb glaze such as the tricolored glaze used in the Nara period (AD 710–794) (Saito, 2001b; Takahashi, 2001b). Mineral assemblage and chemical compositions of ore minerals from the mine were investigated in order to clarify its characteristics as a skarn deposit (Kato, 1916, 1937; Nagashima *et al.*, 2021). Other mines with metal deposits in the area are the Akaono silver-copper and Kitabira mines (Fig. 1). These deposits are found mainly in Paleozoic accretionary complexes comprising the Akiyoshi Limestone Group, which makes up the Akiyoshi Plateau, and they were generated by the intrusion of Cretaceous granite and small dikes into the limestone (Ikeda, 2004; Kato, 1916, 1937; Ogura, 1921; Watanabe, 2009).

As most economic skarn deposits are related to

*Corresponding author: T. Imaoka, imaoka@yamaguchi-u.ac.jp
1) Graduate School of Science and Technology for Innovation, Yamaguchi University, 1677-1 Yoshida, Yamaguchi 753-8512, Japan
2) Department of Earth and Planetary Systems Science, Hiroshima University, 1-3-1 Kagamiyama, Higashi-Hiroshima 739-8526, Japan
3) Hiruzen Institute for Geology and Chronology Co., Ltd., 2-5 Nakashima, Naka-ku, Okayama 703-8252, Japan
4) Koga City Office, 1-1-1 Ekihigashi, Koga, Fukuoka 811-3192, Japan

Received on March 29, 2022; Accepted on July 12, 2022.

magmatic intrusions, the understanding of petrogenesis and tectonic setting of igneous rocks is essential for exploration (Meinert, 1995; Meinert *et al.*, 2005). Geochronological constraints on both intrusive and associated skarns are critical to assess the timing and duration of ore-forming processes (Meinert *et al.*, 2005). However, little is known about the Cu deposits, especially with regards to their age, origin of ore-forming magma of the Hanano-yama pluton, and potential source rocks has not yet been studied in detail, even though it also contributed to the formation of the Naganobori mine.

The present paper reveals of the petrography, mineral chemistry and U–Pb zircon age of the Hanano-yama pluton to assess nature of the magma and timing of formation of the mineralized pluton and metallogeny, and to determine what metallogenic province it belongs to.

2. Geological setting and description of the mines

2.1. Regional geology

From the metallogenic viewpoint, the Inner Zone of SW Japan is divided into the three provinces: from the Median Tectonic Line toward the Sea of Japan side, Barren, Tungsten (W) and Molybdenum (Mo) provinces (Ishihara, 1977, 1981). The Barren Province correspond to the granitoid belt of ilmenite-series Ryoke Belt, whereas the W and Mo provinces to the ilmenite-series San-yo Belt and magnetite-series San-in Belt, respectively (Fig. 1a; Ishihara, 1977; Imaoka and Iizumi, 2009; Nakajima *et al.*, 2016). The study area belongs to the W Province, and is located around the Akiyoshi Plateau in Yamaguchi Prefecture, western part of the Honshu, SW Japan (Fig. 1a). In and around the Akiyoshi Plateau, the Akiyoshi Limestone Group, the Ota Group, and the Tsunemori Formation of the Permian accretionary complex are found mainly with the Triassic Mine Group located in the northwest, the Early Cretaceous Kanmon Group in the north, and the Late Cretaceous Abu Group in the northeast (Fig. 1b). Small Cretaceous igneous intrusions are also present in the Akiyoshi Limestone Group (Ota, 1976; Sasaki *et al.*, 2014, 2016).

The Akiyoshi Limestone Group is composed of Carboniferous to Permian basalts (greenstones) overlain by shallow-water limestones (Ota, 1976). The greenstones have a narrow distribution from the east of Ueyama, through the southwest of Naganobori, to Akiyoshi, whereas the overlying limestone is widespread over the Akiyoshi Plateau (Fig. 1b). The formation age of the greenstones is early Carboniferous, based on fossil ages

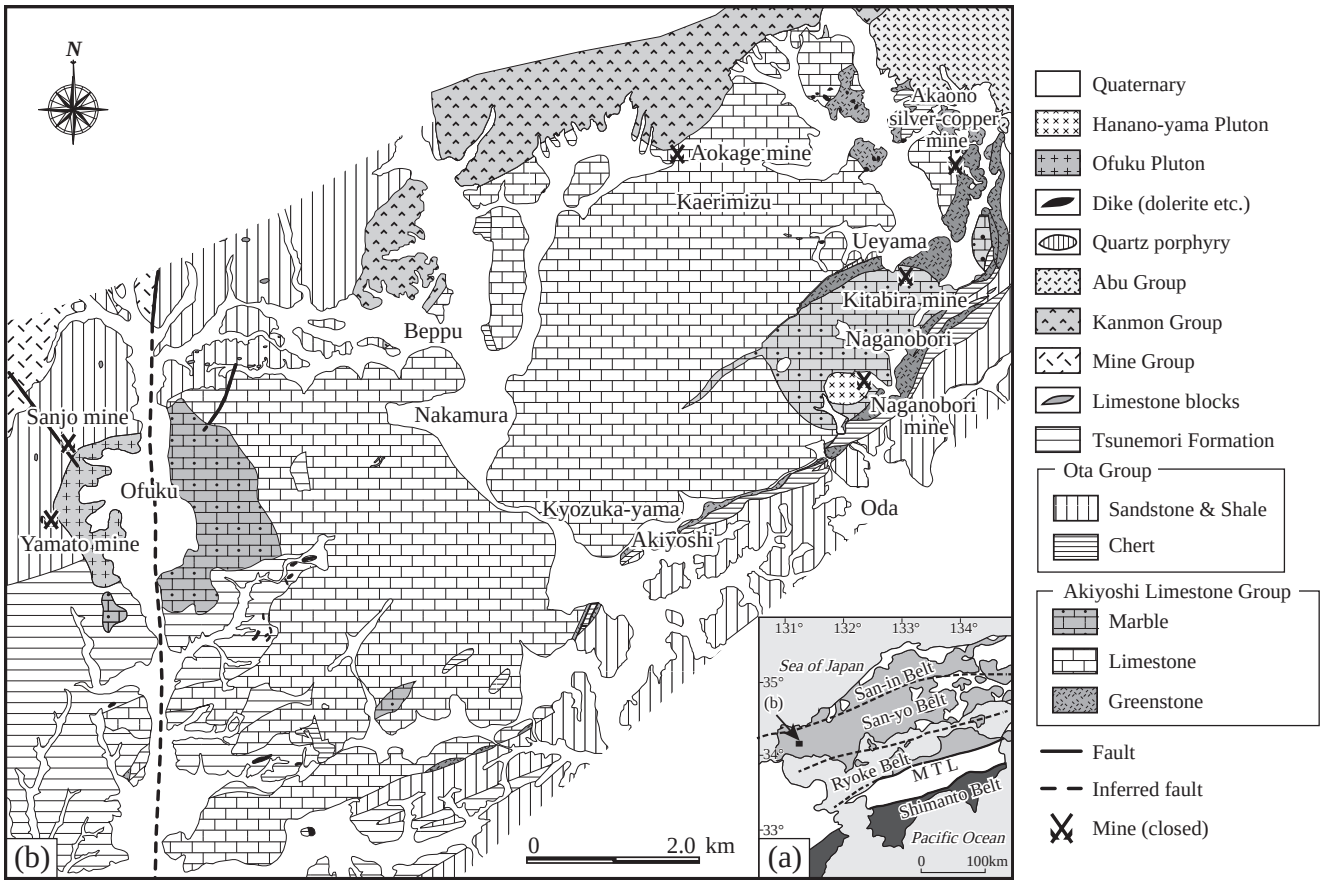

Fig. 1 (a) Division of the Inner Zone of SW Japan. The Ryoke, San-yo, San-in belts correspond to the Barren, W and Mo provinces, respectively, from the metallogenic viewpoint. (b) Geological map of the Akiyoshi Plateau and surrounding area. Modified from Ota (1976).

for overlying limestones (Ota, 1976). The Akiyoshi greenstones are representative of a paleo-oceanic seamount or oceanic island fragments formed by the Carboniferous mantle plume activity (Tatsumi *et al.*, 2000; Sano *et al.*, 2000). The limestone in the area is recrystallized into marble or converted into skarns as observed in the peripheral part of the Hanano-yama pluton (Fig. 1b).

The Ota Group, located in the southeast and south of Oda, around Akiyoshi, and the northwest of the studied area, consists mainly of chert, sandstone, and mudstone. The Tsunemori Formation, located in the southwest of the Akiyoshi Plateau, consists of Permian mudstones and limestones (Fig. 1b) (Ota, 1976).

The Cretaceous Hanano-yama pluton located in the San-yo Belt, occurs in the Naganobori area of Mine City, SW Japan (Fig. 1a). At Mt. Hanano-yama (elevation 310 m), southeastern margin of the Akiyoshi Plateau, a small stock of the Hanano-yama pluton with a surface area of approximately 770 m (east–west) × 510 m (north–south) intrudes the Akiyoshi Limestone Group (Fig 1b, Japan Mining Industry Association, 1965; Ishihara *et al.*, 1984; Nakano and Ishihara, 2003).

Small dikes are present in and around the Akiyoshi Plateau (Fig. 1b). In particular, a discontinuous plagiophyre dike extends from east to west in the area west of Kaerimizu to Ueyama, forming a topographic recess, since the dike rock is more susceptible to weathering than the host rock. Another dike of doleritic composition occurs in the Akiyoshi Plateau (Sasaki *et al.*, 2014). A small dioritic dike is also present at Mt. Kyozuka-yama, Akiyoshi, and Kitabira mining area, which are responsible for the contact metamorphism in the surrounding area, producing marble (Fig. 1b).

2.2. Description of the Naganobori copper mine

The Cu deposits studied here include the Naganobori copper, Kitabira and Akaono silver-copper mines in the eastern part of the Akiyoshi Plateau, and the Yamato mine in the west part of the plateau (Fig. 1b, Nagashima *et al.*, 2015; 2021 and references therein; Sasaki *et al.*, 2016 and references therein). Characteristic features for the Naganobori copper mine are summarized as follows.

The Naganobori copper mine is a proximal skarn deposit of Cu-Zn-(Co)-W, and consists of several ore deposits, such as the Imori (Naganobori), Hakushiki, Ogiri, Umegakubo, Oda, and Eboshi deposits. These deposits are located along the boundary between the granite porphyry of the Hanano-yama pluton and the Akiyoshi Limestone Group, and/or in the limestone near the pluton, indicating close spatial association between the ore zones and igneous rocks. The Imori deposit, formerly known as the Naganobori deposit, occurs along the bedding plane between the limestone and greenstone (e.g., Kato, 1916, Ikeda, 2015). The mine is known as excavated for a long time from the 8th century to 1960 with repeated shutdown of operation, producing Cu and Co (Ogura, 1921; Nakamura, 1954; Ueda, 2002). Cobalt concentration in the Eboshi deposit was found in 1908, and Co-rich ores with more than 10 wt.% Co were mined in the history (Nakamura, 1954). The mining area and copper ore smelting site has been designated as one of Special Historic Sites of Japan in 2003.

The main ore minerals of the mine are chalcopyrite, pyrite, pyrrhotite, and arsenopyrite with subordinate amounts of bornite, cobaltite, sphalerite, galena, and magnetite. At the Eboshi and Imori deposits, cobaltite, bismuthinite, native bismuth, electrum, stannoidite, mawsonite, wittichenite, emplectite, tsumoite, kawazulite, hessite, matildite, pavonite, joseite, and scheelite occur (Watanabe, 2009; Nagashima *et al.*, 2021). The cobaltite has been reported only from the Eboshi and the Imori deposits, and black cobalt oxide (Kato, 1916) corresponds to heterogenite described by Nambu *et al.* (1970). As gangue minerals, hedenbergite, garnet, iron wollastonite, quartz, calcite, and fluorite also occur (Watanabe, 2009). Recently, mineral assemblages and chemical compositions of ore minerals from the Eboshi deposit were reported by Nagashima *et al.* (2021), and some Bi-, Ag-, and Te-bearing minerals are newly identified.

3. Experimental procedures

3.1. Sample and chemical analysis of constituent minerals

Sample NGA-10 is collected at the southeast of the Mt. Hanano-yama (Sampling locality: 34.243085 N, 131.335582 E). The chemical compositions of the constituent minerals of NGA-10 specimen were determined using a JEOL JXA-8230 electron microprobe analyzer at the Centre for Instrumental Analysis, Yamaguchi University, Japan. Operating conditions were: accelerating voltage of 15 kV, a beam current of 20 nA and a beam diameter of 1–5 μm. Wavelength-dispersive X-ray spectra were measured with LiF, PET and TAP monochromators to identify interfering elements and locate the best wave lengths for background measurements. The abundances of Si, Ti, Al, Cr, V, Fe, Mn, Mg, Ca, Ba, Sr, Na, K, P, Ni, Zr, Hf, Sn, Nb, Ta, Th, U, F, Cl and rare-earth elements (REEs: Sc, Y, La, Ce, Pr, Nd, Sm, Eu, and Lu) were measured. Peak positions and background positions of each element were carefully confirmed to avoid their overlap. Several elements, which are not shown in Table 1, are below the detection limit. The probe standards for the measured elements are as

follows; wollastonite (Si, Ca), rutile (Ti), corundum (Al), eskolaite (Cr), $Ca_3(VO_4)_2$ (V), hematite (Fe), manganosite (Mn), periclase (Mg), $SrBaNb_4O_{12}$ (Sr, Ba, Nb), albite (Na), K-feldspar (K), $KTiOPO_4$ (P), NiO (Ni), $(Zr,Y)O_2$ (Zr, Y), Sc-metal (Sc), Hf-metal (Hf), SnO_2 (Sn), Ta-metal (Ta), uranothorite (Th, U), fluorite (F), and halite (Cl). The following standards and X-rays for lanthanoid were used: synthetic REE-bearing hexaborides, $REEB_6$, for La, Ce, Pr, and Nd; synthetic REE-bearing phosphate standards for Sm, Eu, and Lu. The ZAF correction-method was used for all elements.

3.2. Sample preparation and analytical procedures for U–Pb dating

Zircon grains were separated from sample NGA-10 by hand picking following panning whole rock powder in water. The picked grains were mounted in epoxy resin on a glass slide together with zircon standard FC1 ($^{207}Pb/^{206}Pb$ age of 1099.0 ± 0.6 Ma; Paces and Miller, 1993) and zircon consistency standard KO1 (TIMS $^{206}Pb/^{238}U$ age of 95.6 Ma; Herzig *et al.*, 1998). The mounts were then polished until the cores of most of the zircon grains were exposed. Photomicrographs of the zircon grains were taken in both transmitted and reflected light using an optical microscope, and cathodoluminescence (CL) images were captured using a scanning electron microscope (SEM: JEOL JSM-7500F). Analytical points were selected using the photomicrographs and CL images, avoiding mineral inclusions. The images were also used to assess internal structure. Zircon U–Pb isotope analysis was performed using a 213 nm Nd-YAG Laser (New Wave Research UP-213) coupled with an Agilent 7500 ICP–MS at the Department of Earth and Planetary Systems Science, Hiroshima University, Japan. The analytical methodology used was that described by Katsube *et al.* (2012); i.e., a mixed He–N_2–Ar carrier gas system equipped with small volume ablation cell, sample aerosol stabilizer (buffering chamber) and charcoal filter attachment. The laser spot size was 25 μm. Raw data were processed using the data reduction program Pepi-AGE (Dunkl *et al.*, 2008), and final statistical plotting used Isoplot/Ex (Version 3.00; Ludwig, 2003). The isotopic ratios and ages are quoted at 2σ, whereas the weighted mean is given at the 95% confidence level. During this analytical session, the weighted mean $^{206}Pb/^{238}U$ age from eleven spots of zircon standard KO1 was 95.5 ± 1.4 Ma.

4. Petrography and mineral chemistry of dated rock

A photomicrograph of representative sample of the Hanano-yama pluton is shown in Fig. 2. Granite porphyry has a porphyritic hypidiomorphic texture. Phenocrysts are mainly composed of plagioclase, quartz, K-feldspar, and small amounts of biotite, and ilmenite.

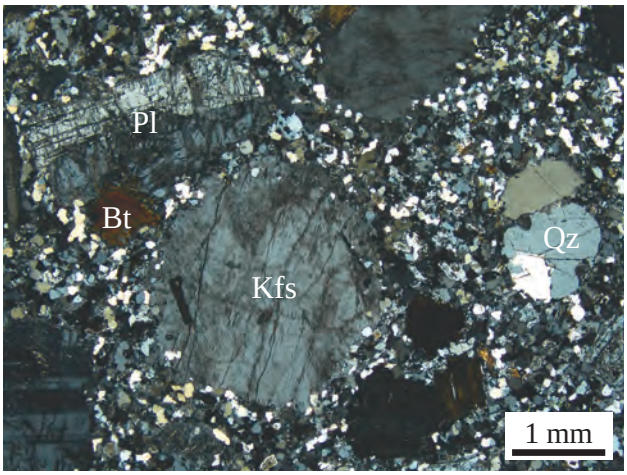

Fig. 2 Photomicrograph (under cross-polarized light) of dated rock sample of the Hanano-yama pluton. Granite porphyry(NGA-10), Qz=quartz, Pl=plagioclase, Kfs= K-feldspar, Bt = biotite.

Back-scattered electron (BSE) images of rock-forming minerals of the Hanano-yama granite porphyry (NGA-10) are presented in Fig. 3. Plagioclase phenocrysts (1–3 mm) are euhedral to subhedral, and the most abundant, and are generally zoned and turbid (Fig. 3a). They have distinct normal zoning from $An_{18–50}$ in the core to $An_{5–15}$ in the rim (Table 1). In the interior part of the plagioclase, the partial melted parts (dusty part) are observed (Fig. 3a). The phenocrysts often have thin marginal rim carrying tiny inclusions of quartz and biotite.

Quartz phenocrysts (usually 1–5 mm, up to 8 mm) are euhedral to anhedral. K-feldspar phenocrysts (0.5–5 mm) are euhedral to subhedral, and contain minute quartz in the peripheral parts of phenocrysts. The mole ratio of orthoclase in K-feldspar is 0.91–0.97 (Table 1).

Biotite phenocrysts (0.2–1.5 mm) are euhedral–subhedral, and pleochroic from X = pale yellow, Z = brown. They occur as single flakes and in intergrowth with ilmenite, and are frequently altered into chlorite and minute epidote. Biotite has a Mg/(Mg + Fe + Mn) ratio of 0.31–0.33, and TiO_2 content of 2.3–3.4 wt.% (Table 1). Average F and Cl contents of biotite is 0.41 wt.%, and 0.25 wt.%, respectively, and some of it contains up to 0.58 wt.% F and up to 0.29 wt.% Cl (Table 1). Some biotites are partially or completely replaced by green chlorite.

Groundmass is composed of anhedral quartz, K-feldspar and plagioclase, and minute ilmenite, titanite, rutile, monazite, allanite, zircon, apatite, thorite and pyrite.

Ilmenite (5–90 μm) is the major Ti-phase, and it is usually found as euhedral to subhedral single grains along the cleavage of biotite and chlorite (chloritized biotite)

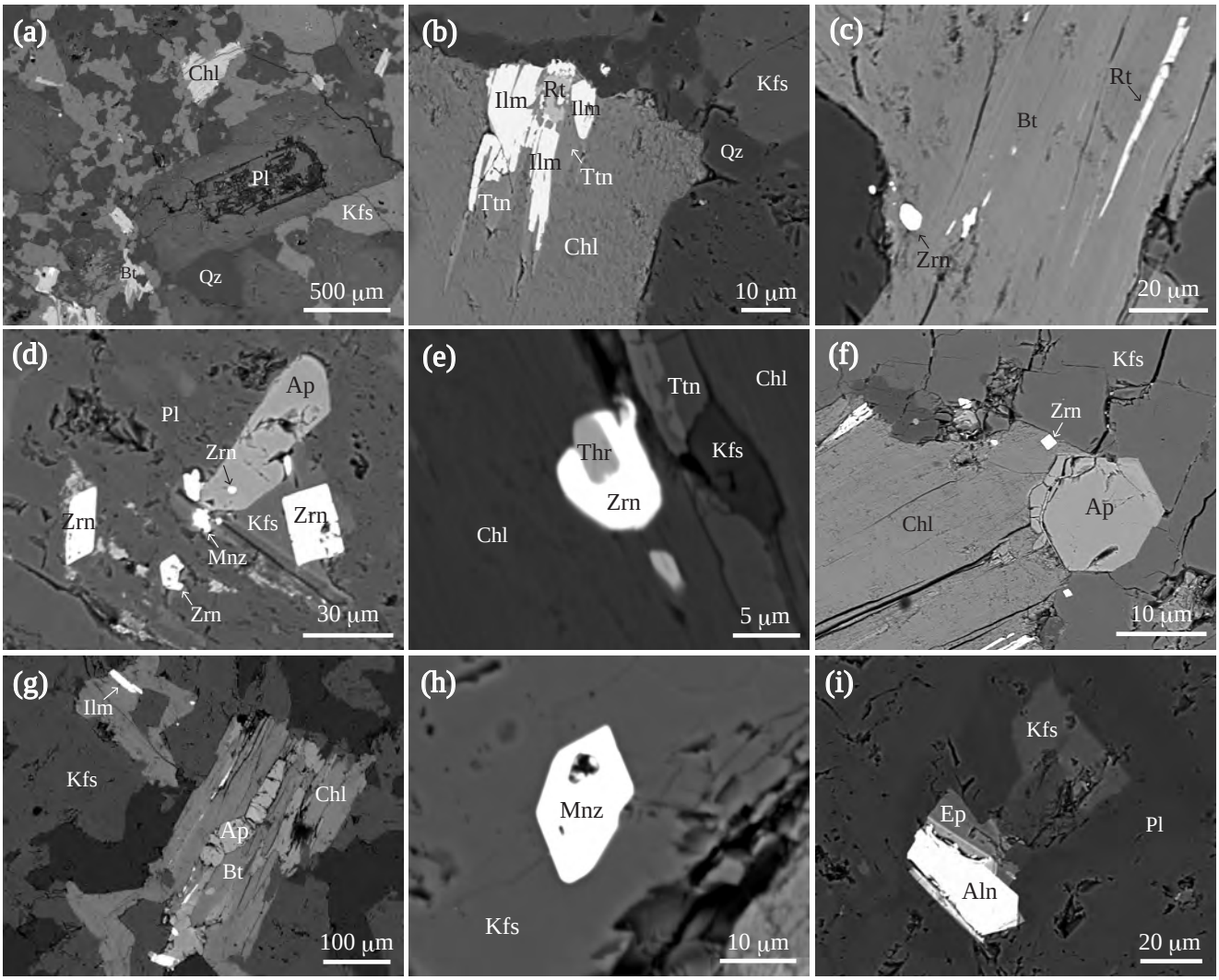

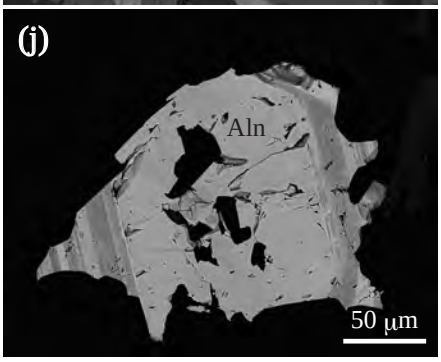

Fig. 3 Back-scattered electron (BSE) images of the constituent minerals of NGA-10 specimen. (a) Plagioclase phenocryst with distinct zoning from $An_{18–50}$ in the core and $An_{5–15}$ in the rim. Core is characterized by dusty inclusion suggesting magma mixing. (b) Ilmenite, rutile and titanite in chloritized biotite. Ilmenite and titanite occur along the cleavage of chloritized biotite. Titanite is rich in F (max. 4.42 wt.%) and Al (max. 13.0 wt.%) and called F-bearing titanite. (c) Rutile needle along the cleavage of biotite. F-bearing biotite (max. 0.58 wt. %) is characteristic in the Hanano-yama pluton. (d) Anhedral monazite and apatite with minute zircon inclusion. (e) Thorite is closely associated with zircon. (f) Euhedral apatite in chloritized biotite. Apatite is rich in F (max. 4.11 wt.%) and LREE, and called fluorapatite. (g) Anhedral apatite in biotite. (h) Euhedral monazite in K-feldspar with abundant F (max. 0.67 wt.%), LREE and Th contents. (i) Allanite and epidote. (j) Anhedral allanite with oscillatory chemical zoning in the rim part, and it is characterized by high contents of F (max. 0.40 wt.%), REE, Ti, Fe^{3+} and Th and F. Abbreviations for names of rock-forming minerals follow Whitney and Evans (2010): Qz = quartz, Pl = plagioclase, Kfs = K-feldspar, Bt = biotite, Chl = chlorite, Aln = allanite, Ep = epidote, Ilm = ilmenite, Ttn = titanite, Rt = rutile, Zrn = zircon, Mnz = monazite, Thr = thorite, Ap = apatite.

(Fig. 3b). It also occurs closely associated with titanite and rutile as anhedral small grains (10–20 μm). Ilmenite is characterized by high Mn content, and its composition ranges $Ilm_{88.5\text{-}80.0}Pph_{11.5\text{-}20.0}$.

Titanite occurs as euhedral to subhedral grain of ~10–160 μm and as highly irregularly distributed grains (Fig. 3b). It is rich in F (up to 4.42 wt.%) and Al_2O_3 (up to 13.0 wt.%), and poor in Cl (up to 0.12 wt.%), and called F-bearing titanite (Table 2). The empirical formula of titanite calculated on the basis of Σcations = 3 is as follows; $Ca_{0.99}(Ti_{0.58}Al_{0.38}Fe_{0.03})_{\Sigma 0.99}Si_{1.01}O_4F_{0.28}(OH)_{0.70}$ (n = 10).

Rutile occurs as acicular crystals (up to 70 μm long) along the cleavage of biotite and chlorite (Fig. 3c), and rarely as anhedral grain associated with ilmenite (Fig. 3b).

Zircon commonly occurs in biotite as euhedral and subhedral grain of ~10 to 90 μm (Fig. 3c, d), and it is

Table 1 Average chemical compositions of plagioclase, K-feldspar and biotite.

	Plagioclase		K-feldspar		Biotite		
	Average	Range	Average	Range	Average	Std	Range
	n = 78		*n* = 29		*n* = 22		
SiO_2	59.39	54.73–65.29	63.06	62.15–65.07	33.94	0.43	33.38–34.72
TiO_2	0.03	0.00–0.16	0.03	0.00–0.12	2.75	0.29	2.33–3.36
Al_2O_3	24.02	19.60–27.35	18.39	17.69–18.86	14.78	0.34	14.33–15.80
Cr_2O_3	0.01	0.00–0.06	0.02	0.00–0.08	0.01	0.02	0.00–0.08
V_2O_3	0.01	0.00–0.10	0.02	0.00–0.08	0.04	0.03	0.00–0.12
FeO	0.08	0.00–2.03	0.12	0.00–0.58	24.8	0.50	23.97–25.72
MnO	0.01	0.00–0.04	0.01	0.00–0.03	0.47	0.05	0.40–0.58
MgO	0.01	0.00–0.09	0.00	0.00–0.02	6.68	0.13	6.45–6.89
CaO	5.74	0.83–9.61	0.03	0.00–0.09	0.01	0.01	0.00–0.04
BaO	0.04	0.00–0.18	0.24	0.00–1.17	0.51	0.18	0.14–0.81
SrO	0.00	0.00–0.04	0.00	0.00–0.08	0.01	0.02	0.00–0.05
Na_2O	7.53	4.95–10.75	0.67	0.28–0.98	0.25	0.09	0.10–0.43
K_2O	0.48	0.08–0.95	16.35	14.65–17.46	9.8	0.23	9.38–10.15
P_2O_5	0.01	0.00–0.10	0.01	0.00–0.05	0.01	0.01	0.00–0.03
F	-		-		0.41	0.08	0.27–0.58
Cl	-		-		0.25	0.02	0.20–0.29
Total	97.36		98.95		94.72		
Ex.O	-		-		0.23		
Total-Ex.O	97.36		98.95		94.49		
Normalized as	O = 8		O = 8		O = 22		
Si	2.71	2.47–2.95	2.97	2.94–2.99	5.46	0.03	5.38–5.50
Ti	0.00	0.00–0.01	0.00	0.00–0.00	0.33	0.03	0.28–0.41
Al	1.29	1.06–1.48	1.02	0.99–1.05	2.80	0.06	2.70–2.96
Cr^{3+}	0.00	-	0.00	-	0.00	0.00	0.00–0.01
V^{3+}	0.00	-	0.00	-	0.00	0.00	0.00–0.01
Fe^{2+}	0.00	0.00–0.08	0.00	0.00–0.02	3.33	0.07	3.22–3.48
Mn^{2+}	0.00	-	0.00	-	0.06	0.01	0.05–0.08
Mg	0.00	0.00–0.01	0.00	-	1.60	0.03	1.54–1.65
Ca	0.28	0.04–0.47	0.00	-	0.00	0.00	0.00–0.01
Ba	0.00	-	0.00	0.00–0.02	0.03	0.01	0.01–0.05
Sr	0.00	-	0.00	-	0.00	0.00	0.00–0.01
Na	0.67	0.44–0.94	0.06	0.03–0.09	0.08	0.03	0.03–0.13
K	0.03	0.00–0.05	0.98	0.89–1.05	2.01	0.04	1.93–2.10
P	0.00	-	0.00	-	0.00	0.00	-
Total	4.98		5.03		15.70		-
F	-		-		0.21	0.04	0.14–0.29
Cl	-		-		0.07	0.01	0.05–0.08
An: $CaAl_2Si_2O_8$	28.7	4.6–50.5	0.1	0.0–0.4	Mg/(Mg+Fe+Mn)		
Ab: $NaAlSi_3O_8$	68.5	48.3–94.5	5.8	2.6–8.5	0.32		0.31–0.33
Or: $KAlSi_3O_8$	2.8	0.5–5.7	94.0	91.1–97.4			

sometimes closely associated with thorite (Fig. 3e). The Zr content decreases with increasing Hf content. HfO_2 content attains 3.5 wt.% (Table 2). A BSE image reveals the presence of zircon inclusion of about 3 μm in apatite, suggesting that the zircon crystallized prior to apatite (Fig. 3d).

Thorite occurs as small anhedral grain of ~20 μm in size, which is often closely associated with zircon (Fig. 3e), and also sometimes with apatite.

Apatite (10–250 μm long) occurs as euhedral–subhedral (Fig. 3d, f), and acicular and/or columnar crystals in biotite and chlorite (Fig. 3g), which is considered to result from rapid cooling (Wyllie *et al.*, 1962). As a result of the chemical analysis, fluorine predominates over chlorine in all analyzed grains (2.1–4.1 wt.% F and 0.1–0.5 wt.% Cl). Cl content of apatite here is

Table 2 Average chemical compositions of REE-bearing accessory minerals.

	Titanite			Zircon			Fluorapatite			Monazite-(Ce)			Allanite-(Ce)*		
	Ave.	Std.	Range	Ave.	Std.	Range	Ave.	Std.	Range	Ave.	Std.	Range	Ave.	Std.	Range
	n = 10			n = 54			n = 26			n = 7			n = 35		
SiO_2	30.43	0.40	29.91–31.01	31.27	0.92	29.57–33.67	0.16	0.09	0.05–0.50	1.74	0.40	1.13–2.34	30.55	0.79	29.52–32.90
TiO_2	23.19	2.11	19.97–26.27	0.08	0.08	0.00–0.27	0.04	0.05	0.00–0.18	0.07	0.09	0.00–0.27	0.74	0.48	0.18–2.55
Al_2O_3	9.63	1.25	8.52–12.95	0.06	0.09	0.00–0.43	0.02	0.01	0.00–0.04	0.03	0.04	0.00–0.10	15.06	1.17	11.63–17.48
Cr_2O_3	0.02	0.03	0.00–0.07	0.02	0.03	0.00–0.11	0.02	0.03	0.00–0.10	0.00	0.00	0.00	0.00	0.00	0.00
V_2O_3	0.12	0.06	0.00–0.18	0.02	0.03	0.00–0.13	0.02	0.02	0.00–0.07	0.00	0.00	0.00	0.02	0.02	0.00–0.08
FeO	1.03	0.47	0.30–1.71	0.39	0.44	0.00–1.63	0.37	0.20	0.07–0.85	0.15	0.14	0.00–0.38	13.92	0.92	12.22–15.91
MnO	0.03	0.03	0.00–0.09	0.01	0.02	0.00–0.06	0.38	0.13	0.15–0.78	0.00	0.00	0.00	0.48	0.25	0.05–0.89
MgO	0.05	0.03	0.02–0.10	0.02	0.02	0.00–0.09	0.01	0.02	0.00–0.07	0.01	0.01	0.00–0.03	0.37	0.09	0.17–0.59
CaO	28.05	0.27	27.70–28.58	0.06	0.05	0.00–0.21	52.81	0.76	51.16–53.82	0.63	0.31	0.21–1.04	10.13	0.74	9.20–12.43
BaO	0.09	0.07	0.00–0.19	0.04	0.06	0.00–0.30	0.05	0.06	0.00–0.22	0.06	0.05	0.00–0.13	0.03	0.04	0.00–0.17
SrO	0.00	0.00	0.00	0.06	0.05	0.00–0.22	0.00	0.00	0.00	0.02	0.03	0.00–0.07	0.00	0.01	0.00–0.04
Na_2O	0.03	0.05	0.00–0.15	0.02	0.02	0.00–0.12	0.09	0.03	0.04–0.15	0.00	0.00	0.00	0.00	0.00	0.00–0.02
K_2O	0.04	0.06	0.00–0.18	0.07	0.10	0.00–0.53	0.04	0.06	0.00–0.28	0.27	0.16	0.08–0.58	0.03	0.07	0.00–0.24
P_2O_5	0.02	0.01	0.00–0.04	0.59	0.56	0.00–1.61	40.24	0.86	38.35–41.50	26.20	1.52	24.03–27.91	0.02	0.02	0.00–0.07
NiO	0.11	0.14	0.00–0.35	0.09	0.16	0.00–0.57	0.07	0.11	0.00–0.31	0.05	0.09	0.00–0.23	0.10	0.16	0.00–0.39
ZrO_2	0.00	0.01	0.00–0.02	60.73	2.41	56.01–66.30	0.00	0.00	0.00–0.00	0.00	0.00	0.00	0.01	0.01	0.00–0.03
HfO_2	0.03	0.06	0.00–0.18	1.71	0.79	0.76–3.46	0.05	0.08	0.00–0.28	0.04	0.06	0.00–0.13	0.05	0.06	0.00–0.22
SnO_2	0.00	0.01	0.00–0.02	0.01	0.01	0.00–0.05	0.00	0.00	0.00–0.01	0.00	0.00	0.00	0.00	0.00	0.00–0.01
Sc_2O_3	0.01	0.02	0.00–0.05	0.06	0.05	0.00–0.20	0.00	0.00	0.00	0.00	0.00	0.00	0.02	0.02	0.00–0.08
Y_2O_3	0.01	0.02	0.00–0.05	0.83	0.75	0.00–2.67	0.31	0.11	0.16–0.58	1.99	1.30	0.88–3.90	1.06	0.50	0.22–2.71
La_2O_3	0.00	0.00	0.00	0.01	0.03	0.00–0.14	0.05	0.05	0.00–0.22	11.55	1.39	9.71–13.33	4.93	0.48	3.52–5.74
Ce_2O_3	0.02	0.04	0.00–0.10	0.05	0.05	0.00–0.23	0.24	0.06	0.14–0.38	27.21	1.90	24.33–29.45	10.77	0.91	7.14–12.16
Pr_2O_3	0.00	0.00	0.00–0.01	0.03	0.03	0.00–0.12	0.03	0.04	0.00–0.18	4.75	0.28	4.35–5.10	1.83	0.18	1.25–2.21
Nd_2O_3	0.00	0.01	0.00–0.02	0.03	0.03	0.00–0.14	0.17	0.05	0.05–0.26	11.14	1.44	9.75–13.71	4.24	0.39	3.25–4.67
Sm_2O_3	0.01	0.01	0.00–0.04	0.02	0.04	0.00–0.17	0.05	0.05	0.00–0.17	2.87	0.63	2.08–3.72	1.02	0.22	0.41–1.50
Eu_2O_3	0.03	0.05	0.00–0.12	0.05	0.09	0.00–0.41	0.05	0.08	0.00–0.31	0.52	0.30	0.11–0.90	0.24	0.12	0.00–0.50
Lu_2O_3	0.04	0.10	0.00–0.32	0.18	0.17	0.00–0.53	0.00	0.00	0.00	0.23	0.20	0.00–0.49	0.14	0.17	0.00–0.48
Nb_2O_5	0.12	0.09	0.03–0.35	0.01	0.02	0.00–0.11	0.02	0.02	0.00–0.05	0.00	0.00	0.00	0.01	0.02	0.00–0.06
Ta_2O_5	0.05	0.07	0.00–0.17	0.05	0.09	0.00–0.39	0.04	0.06	0.00–0.23	0.00	0.00	0.00	0.15	0.23	0.00–0.92
ThO_2	0.00	0.01	0.00–0.03	0.24	0.28	0.00–1.36	0.01	0.01	0.00–0.05	6.43	2.07	3.21–8.32	0.13	0.16	0.00–0.52
UO_2	0.00	0.01	0.00–0.03	0.69	0.56	0.00–2.19	0.01	0.02	0.00–0.06	0.50	0.21	0.18–0.84	0.02	0.03	0.00–0.11
F	2.63	0.82	1.72–4.42	0.07	0.07	0.00–0.31	2.96	0.53	2.13–4.11	0.58	0.06	0.48–0.67	0.18	0.10	0.00–0.40
Cl	0.02	0.04	0.00–0.12	0.00	0.00	0.00–0.01	0.29	0.08	0.09–0.51	0.03	0.01	0.03–0.04	0.02	0.01	0.01–0.04
Total	95.84			97.56			98.58			97.05			96.26		
Ex.O	1.11			0.03			1.31			0.25			0.08		
Total-Ex.O	94.73			97.53			97.27			96.80			96.18		
Normalized as	Total cations = 3			O = 4			Total cations = 8			O = 4			Total cations = 8		
Si	1.01	0.01	0.99–1.03	0.99	0.02	0.96–1.03	0.01	0.01	0.00–0.04	0.07	0.02	0.05–0.10	3.00	0.03	2.95–3.05
Ti	0.58	0.05	0.49–0.65	0.00	0.00	0.00–0.01	0.00	0.00	0.00–0.01	0.00	0.00	0.00–0.01	0.05	0.04	0.01–0.19
Al	0.38	0.05	0.33–0.50	0.00	0.00	0.00–0.02	0.00	0.00	-	0.00	0.00	-	1.74	0.11	1.39–1.91
Cr	0.00	0.00	-	0.00	0.00	-	0.00	0.00	0.00–0.01	0.00	0.00	-	0.00	0.00	-
V	0.00	0.00	-	0.00	0.00	-	0.00	0.00	-	0.00	0.00	-	0.00	0.00	-
Fe	0.03	0.01	0.01–0.05	0.01	0.01	0.00–0.04	0.03	0.01	0.01–0.06	0.01	0.00	0.00–0.01	1.14	0.08	1.00–1.32
Mn	0.00	0.00	-	0.00	0.00	-	0.03	0.01	0.01–0.06	0.00	0.00	-	0.04	0.02	0.00–0.07
Mg	0.00	0.00	-	0.00	0.00	-	0.00	0.00	0.00–0.01	0.00	0.00	-	0.05	0.01	0.02–0.09
Ca	0.99	0.01	0.97–1.02	0.00	0.00	0.00–0.01	4.91	0.03	4.87–4.98	0.03	0.01	0.01–0.05	1.07	0.06	0.98–1.25
Ba	0.00	0.00	-	0.00	0.00	-	0.00	0.00	0.00–0.01	0.00	0.00	-	0.00	0.00	0.00–0.01
Sr	0.00	0.00	-	0.00	0.00	-	0.00	0.00	-	0.00	0.00	-	0.00	0.00	-
Na	0.00	0.00	0.00–0.01	0.00	0.00	0.00–0.01	0.02	0.00	0.01–0.03	0.00	0.00	-	0.00	0.00	-
K	0.00	0.00	0.00–0.01	0.00	0.00	0.00–0.02	0.00	0.01	0.00–0.03	0.01	0.01	0.00–0.03	0.00	0.01	0.00–0.03
P	0.00	0.00	-	0.02	0.02	0.00–0.04	2.95	0.03	2.89–3.00	0.91	0.02	0.88–0.93	0.00	0.00	0.00–0.01
Ni	0.00	0.00	0.00–0.01	0.00	0.00	0.00–0.01	0.00	0.01	0.00–0.02	0.00	0.00	0.00–0.01	0.01	0.01	0.00–0.03
Zr	0.00	0.00	-	0.94	0.03	0.89–0.98	0.00	0.00	-	0.00	0.00	-	0.00	0.00	-
Hf	0.00	0.00	-	0.02	0.01	0.01–0.03	0.00	0.00	0.00–0.01	0.00	0.00	-	0.00	0.00	0.00–0.01
Sn	0.00	0.00	-	0.00	0.00	-	0.00	0.00	-	0.00	0.00	-	0.00	0.00	-
Sc	0.00	0.00	-	0.00	0.00	0.00–0.01	0.00	0.00	-	0.00	0.00	-	0.00	0.00	0.00–0.01
Y	0.00	0.00	-	0.01	0.01	0.00–0.05	0.01	0.00	0.01–0.03	0.04	0.03	0.02–0.08	0.06	0.03	0.01–0.14
La	0.00	0.00	-	0.00	0.00	-	0.00	0.00	0.00–0.01	0.17	0.02	0.15–0.21	0.18	0.02	0.12–0.21
Ce	0.00	0.00	-	0.00	0.00	-	0.01	0.00	0.00–0.01	0.41	0.02	0.36–0.43	0.39	0.04	0.25–0.45
Pr	0.00	0.00	-	0.00	0.00	-	0.00	0.00	0.00–0.01	0.07	0.00	0.06–0.07	0.07	0.01	0.04–0.08
Nd	0.00	0.00	-	0.00	0.00	-	0.01	0.00	0.00–0.01	0.16	0.02	0.15–0.19	0.15	0.01	0.11–0.17
Sm	0.00	0.00	-	0.00	0.00	-	0.00	0.00	0.00–0.01	0.04	0.01	0.03–0.05	0.03	0.01	0.01–0.05
Eu	0.00	0.00	-	0.00	0.00	-	0.00	0.00	0.00–0.01	0.01	0.00	0.00–0.01	0.01	0.00	0.00–0.02
Lu	0.00	0.00	-	0.00	0.00	0.00–0.01	0.00	0.00	-	0.00	0.00	0.00–0.01	0.00	0.00	0.00–0.01
Nb	0.00	0.00	0.00–0.01	0.00	0.00	-	0.00	0.00	-	0.00	0.00	-	0.00	0.00	-
Ta	0.00	0.00	-	0.00	0.00	-	0.00	0.00	0.00–0.01	0.00	0.00	-	0.00	0.01	0.00-0.02
Th	0.00	0.00	-	0.00	0.00	0.00–0.01	0.00	0.00	-	0.06	0.02	0.03–0.08	0.00	0.00	0.00-0.01
U	0.00	0.00	-	0.00	0.00	0.00–0.02	0.00	0.00	-	0.00	0.00	0.00–0.01	0.00	0.00	-
Total	3.00			2.01			8.00			1.99			8.00		
F	0.28	0.08	0.18–0.45	0.01	0.01	0.00–0.03	0.81	0.15	0.58–1.14	0.07	0.01	0.06–0.09	0.06	0.03	0.00–0.13
Cl	0.00	0.00	0.00–0.01	0.00	0.00	-	0.04	0.01	0.01–0.08	0.00	0.00	-	0.00	0.00	0.00–0.01

*The Fe^{2+} and Fe^{3+} in allanite-(Ce) is esimated as 0.91 and 0.23 apfu, respectively (Fe^{2+}/total Fe = 0.80). The Fe^{2+}/total Fe varies from 0.68 to 0.89 among 35 analytical points.

poor compared to that of the Ofuku pluton (1.28 wt.% in granite; Sasaki *et al.*, 2016). The empirical formula is represented as $(Ca_{4.91}Mn_{0.03}Fe_{0.03}Na_{0.02}Y_{0.01}Ce_{0.01}Nd_{0.01})_{\Sigma 5.02}(P_{2.95}Si_{0.01})_{\Sigma 2.96}O_{11.84}[F_{0.81}Cl_{0.04}(OH)_{0.31}]$ based on the average chemical composition (n = 26 in Table 2). The OH content is estimated to maintain neutralization of formula, which is obviously less than fluorine. Thus, the studied apatite can be classified into fluorapatite.

The Hanano-yama granite porphyry contains larger amount of monazite-(Ce) and smaller amounts of allanite than the Ofuku pluton. Monazite-(Ce) grains are observed in K-feldspar and quartz as anhedral rounded grain of 2–20 μm in across (Fig. 3d), but rarely occur as euhedral one (Fig. 3h). ThO_2 contents ranges from 3.2 to 8.3 wt.% (Table 2). The second dominant rare-earth element is La (0.15–0.21 apfu based on O = 4) or Nd (0.15–0.19 apfu) though Ce is always most dominant (0.36–0.43 apfu) among REEs (Table 2). The chemical formula based on the average chemical composition is $(Ce_{0.41}La_{0.17}Nd_{0.16}Pr_{0.07}Th_{0.06}Y_{0.04}Sm_{0.04}Eu_{0.01}Ca_{0.03}K_{0.01}Fe_{0.01})_{\Sigma 1.01}(P_{0.91}Si_{0.07})_{\Sigma 0.98}O_4F_{0.07}$ (n = 7) normalized as O = 4. The modal amounts of monazite-(Ce) in the Hanano-yama granite porphyry are larger than those of allanite-(Ce), thus, larger parts of light REE (LREE) are incorporated in monazite-(Ce).

Allanite occurs as euhedral grain (Fig. 3i) and interstitial anhedral grain (120–850 μm in size), and its BSE image shows the presence of oscillatory chemical zoning at the peripheral part of the grain (Fig. 3j). The average chemical formula based on average chemical data (n = 35) based on total number of cations, except H, was normalized to eight is $(Ca_{1.07}Mn^{2+}{}_{0.04}Ce_{0.39}La_{0.18}Nd_{0.15}Pr_{0.07}Y_{0.06}Sm_{0.03}Eu_{0.01})_{\Sigma 2.00}(Al_{1.74}Fe^{2+}{}_{0.91}Fe^{3+}{}_{0.23}Mg_{0.05}Ti_{0.05}Ni_{0.01})_{\Sigma 2.99}Si_{3.00}O_{12}(OH)_{0.94}F_{0.06}$ (Table 2). The Fe^{2+}/total Fe value was calculated based on total positive charge of 25 to maintain charge balance. The Fe^{2+}/total Fe varies 0.68–0.89 among the 35 analytical points. Our analytical data demonstrate that Ce is predominant over other REEs in all allanite grains studied here; they all are, thus, classified into allanite-(Ce). Although titanium is a minor component in general, it is rarely concentrated at the rim of allanite-(Ce). The TiO_2 content attains up to 2.6 wt.% corresponding to 0.19 Ti atoms per formula unit (Table 2). The Ti-rich part is also enriched in Fe, LREE and Th, and tends to be depleted in Si and Al. In addition, epidote associated with allanite-(Ce) was scarcely observed (Fig. 3i). The chemical formula of epidote is represented as $(Ca_{1.98}Ce_{.0.01}Mn_{0.01})_{\Sigma 2.00}(Al_{2.33}Fe^{3+}{}_{0.65}Mg_{0.01}Ni_{0.01})_{\Sigma 3.00}Si_{3.00}O_{12}(OH)_{0.99}F_{0.01}$. The REEs are hardly contained in epidote (up to 1.3 wt.% REE_2O_3) compared to the associated allanite-(Ce), and all iron in epidote is assumed to be ferric.

5. In situ U–Pb dating results of zircon

Photomicrographs and cathodoluminescence (CL) images of the zircon grains are shown in Fig. 4. All analyzed zircon grains are colorless and transparent, and have euhedral shape. Length and length/width ratios for zircons are 150–340 μm and 2.1–4.6, respectively. The CL images show that most zircon grains are characterized by fine-scale oscillatory igneous zoning, reflecting variations in trace element (U, Th, Y, and heavy REE) concentrations.

Result of the LA–ICP–MS U–Pb zircon analyses is listed in Table 3. The zircon Th/U ratios range from 0.17 to 0.62, indicating igneous origin. Fig. 5 shows the Tera–Wasserburg diagram ($^{207}Pb/^{206}Pb$ vs. $^{238}U/^{206}Pb$). Twenty-four spots were analyzed from 12 zircon grains (Figs. 4 and 5). The 21 spots among them showed low discordancy (less than 10%) and their error ellipses are on the concordia line, here referred to as "concordant", and yielded a weighted mean $^{206}Pb/^{238}U$ age of 101.5 ± 0.7 Ma (MSWD = 0.56) (Fig. 6). The dated zircon grains show no significant age differences between cores and rims, and their MSWDs are low. All age determined are interpreted to represent the crystallization age of the magmatic zircons.

6. Discussion

The Cretaceous Hanano-yama pluton is calc-alkaline, ilmenite-series, and occurs in the Tungsten Province of SW Japan. The porphyritic nature of this pluton indicates shallow-level emplacement, and the emplacement of the pluton in the Akiyoshi Limestone Group caused the formation of skarn ore deposits such as the Eboshi, Ogiri, Hakushiki, *etc.* between them (Kato, 1937).

Chemical analysis of rock-forming minerals of the Hanano-yama granite porphyry revealed the existence of F-bearing minerals such as F-bearing biotite (max. 0.58 wt.%, ave. 0.41 wt.% F), titanite (4.42, 2.63 wt.%), fluorapatite (4.11, 2.96 wt.%), monazite-(Ce) (0.67, 0.58 wt.%), allanite-(Ce) (0.40, 0.18 wt.%). REEs are also enriched in monazite-(Ce), allanite-(Ce), fluorapatite, zircon and titanite (Table 2). This suggests that the fluorine and REEs were significantly enriched in the residual melt and fluids during the crystallization of the Hanano-yama pluton. Until recently, hydrothermal transport of the REE in fluorine-bearing ore-forming systems has generally assumed to occur mainly due to the formation of REE-fluoride complexes (e.g., Smith and Henderson, 2000; Williams-Jones *et al.*, 2012). The transportation of REE in magmas and fluids is now hotly debated (e.g., Williams-Jones and Migdisov, 2014,

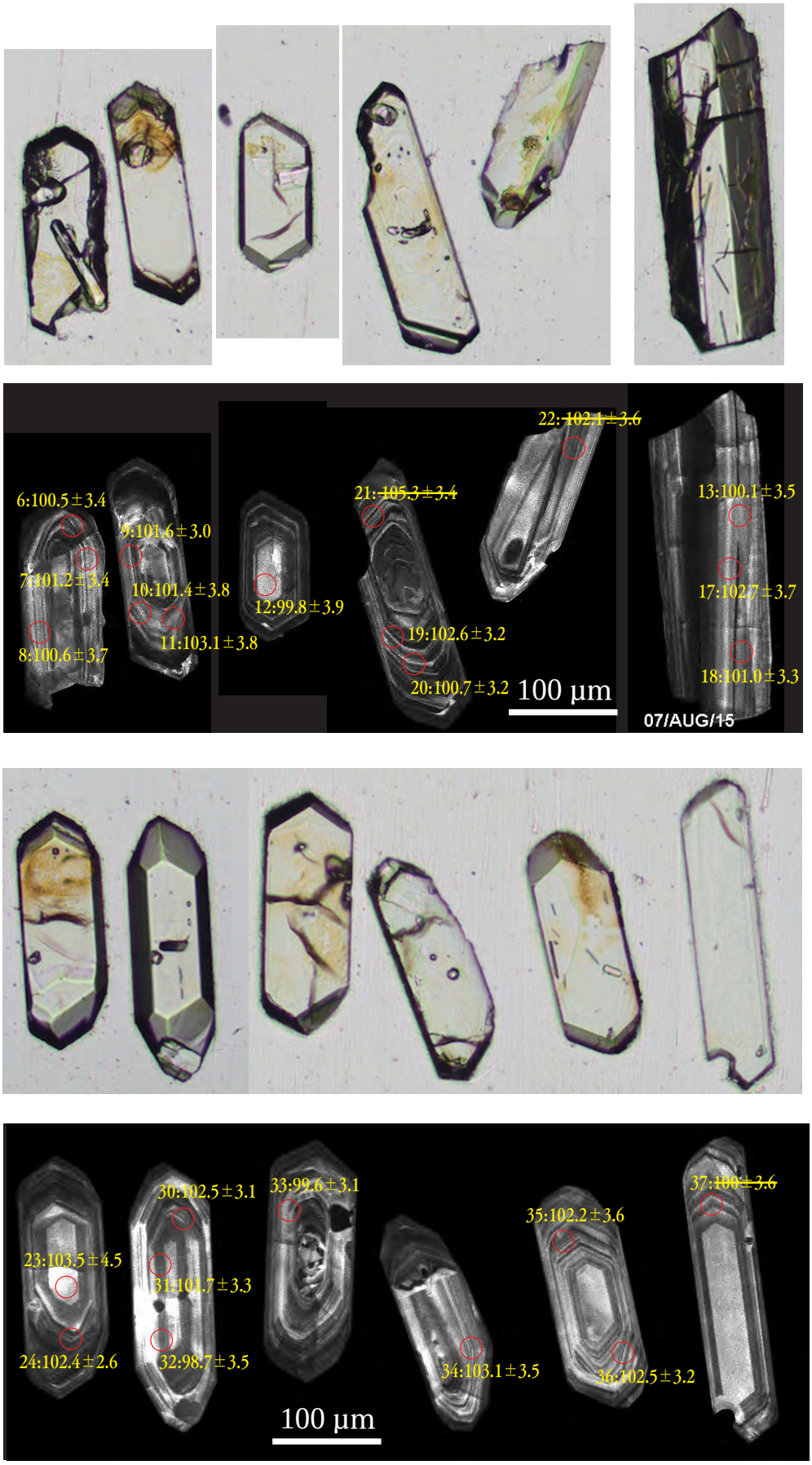

Fig. 4 Photomicrographs and cathodoluminescence (CL) images of 12 zircon grains separated from the Hanano-yama granite porphyry NGA-10. Circles indicate the laser ablation area of ca. 20-µm diameter. 6-37 are the spot label numbers shown in Table 3. Ages with strikethrough are "discordant".

Table 3 LA–ICP–MS zircon U–Pb isotopic data for the Hanano-yama granite porphyry.

Spot Label	$^{238}U/^{206}Pb^{*}$ ± 2σ		$^{207}Pb^{*}/^{206}Pb^{*}$ ± 2σ		$^{206}Pb^{*}/^{238}U$ age ± 2σ (Ma)		$^{207}Pb^{*}/^{235}U$ age ± 2σ (Ma)		$^{207}Pb^{*}/^{206}Pb^{*}$ age ± 2σ (Ma)		Th/U	Disc.[(1)] (%)
6	63.61	2.16	0.0492	0.0042	100.5	3.4	102.9	9.0	158	158	0.472	2.4
7	63.25	2.15	0.0528	0.0051	101.2	3.4	110.6	10.9	320	237	0.558	9.3
8	63.61	2.35	0.0479	0.0073	100.6	3.7	100.2	15.0	92	92	0.404	–0.4
9	62.93	1.89	0.0470	0.0050	101.6	3.0	99.6	10.5	51	51	0.620	–2.0
10	63.05	2.40	0.0457	0.0058	101.4	3.8	96.7	12.2	0	0	0.484	–4.6
11	62.03	2.30	0.0439	0.0058	103.1	3.8	94.5	12.4	0	0	0.382	–8.3
12	64.10	2.50	0.0470	0.0070	99.8	3.9	97.8	14.5	49	49	0.422	–2.0
13	63.94	2.24	0.0472	0.0058	100.1	3.5	98.4	12.1	60	59	0.215	–1.7
17	62.27	2.24	0.0474	0.0069	102.7	3.7	101.4	14.5	70	70	0.250	–1.3
18	63.29	2.09	0.0507	0.0045	101.0	3.3	106.3	9.5	226	217	0.262	5.2
19	62.34	1.93	0.0501	0.0029	102.6	3.2	106.7	6.7	199	141	0.260	4.0
20	63.53	2.03	0.0498	0.0028	100.7	3.2	104.2	6.4	186	136	0.249	3.5
21	60.75	2.00	0.0521	0.0030	105.3	3.4	113.4	7.2	288	138	0.398	7.7
22	62.62	2.25	0.0388	0.0059	102.1	3.6	83.3	12.5	0	0	0.580	–18.4
23	61.80	2.72	0.0476	0.0091	103.5	4.5	102.5	19.4	79	79	0.382	–1.0
24	62.46	1.62	0.0497	0.0028	102.4	2.6	105.7	6.2	181	136	0.172	3.2
30	62.38	1.87	0.0472	0.0034	102.5	3.1	100.7	7.5	58	58	0.333	–1.8
31	62.85	2.07	0.0475	0.0057	101.7	3.3	100.5	12.0	73	73	0.434	–1.2
32	64.81	2.33	0.0445	0.0060	98.7	3.5	91.9	12.3	0	0	0.434	–6.9
33	64.23	1.99	0.0506	0.0036	99.6	3.1	104.7	7.7	221	173	0.215	5.1
34	62.07	2.11	0.0512	0.0054	103.1	3.5	109.4	11.6	251	251	0.433	6.1
35	62.54	2.19	0.0511	0.0051	102.2	3.6	108.4	11.0	245	245	0.395	6.1
36	62.38	1.93	0.0451	0.0046	102.5	3.2	96.5	9.8	0	0	0.422	–5.9
37	63.98	2.30	0.0552	0.0051	100.0	3.6	114.1	10.7	420	220	0.514	14.1

(1) Discordance defined as [($^{207}Pb^{*}/^{235}U$ age)/($^{206}Pb^{*}/^{238}U$ age) – 1] × 100 (%)

* stands for the radiogenic component.

Gray masked data are those having isotope ratio whose error ellipses are detached from concordia line.

See also concordia plot of Fig. 6.

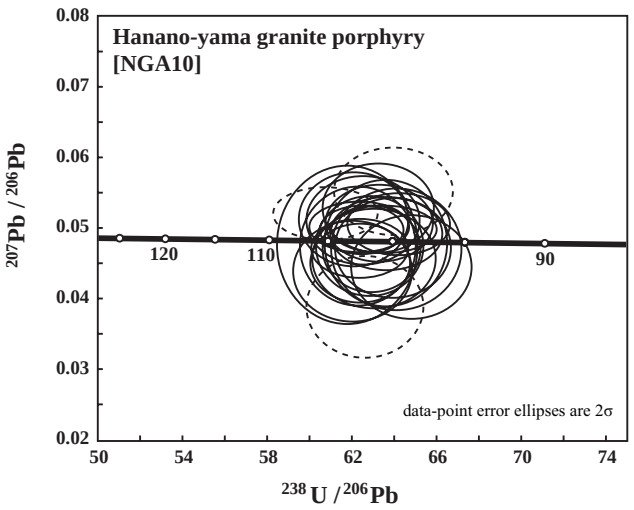

Fig. 5 Tera–Wasserburg diagram ($^{207}Pb/^{206}Pb$ vs. $^{238}U/^{206}Pb$) of the LA–ICP–MS zircon U–Pb isotopic analyses of 12 zircon grains separated from the Hanano-yama granite porphyry NGA-10. The dashed ellipses indicate discordant data.

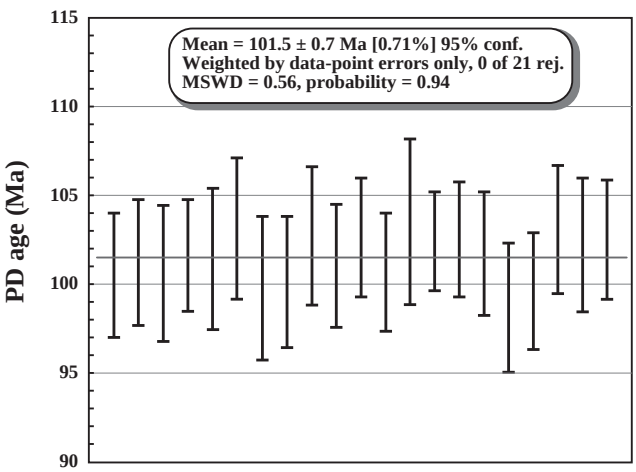

Fig. 6 Weighted average of $^{206}Pb/^{238}U$ age (101.5 ± 0.7 Ma) for 21 concordant spots of the zircons separated from the sample NGA-10.

Verplanck, 2017, Cangelosi, *et al.*, 2020, and references therein).

Magmatic zircons define the crystallization age of the Hanano-yama pluton at 101.5 ± 0.7 Ma. Contemporaneous magmatism related to skarn mineralization yielding K–Ar ages of hornblende (97–99 Ma) and biotite (98–101 Ma) were reported in the Ofuku pluton in the western part of the Akiyoshi Plateau (Sasaki *et al.*, 2016). Similar K–Ar ages were also reported from the skarn deposits in the eastern part of Yamaguchi Prefecture, in major W metallogenic Province of SW Japan. Muscovite separated from the Cu (Pb–Zn) skarns at the Kuga, Kiwada, and Fujigatani mines yielded ages of 94 Ma, 100–102 Ma, and 96 Ma, respectively (Shibata and Ishihara, 1974; Watanabe *et al.*, 1988). These K–Ar ages of the skarns are almost identical to those of the granites occurring as a hidden cupola at the Fujigatani mine (Shibata and Ishihara, 1974) and granitoids widely exposed in the surrounding area (Higashimoto *et al.*, 1983). From these data, mineralization ages of the Sanyo Belt of Yamaguchi Prefecture genetically related to the ilmenite-series granitoids are estimated to be ca. 94 to 102 Ma.

Acknowledgements

Our sincere gratitude goes to Yoshifumi Ikeda, director of Naganobori Copper-mine and Culture Center, for his permission for sample collection and cooperation of field survey. We thank Yoji Morifuku of the Centre for Instrument Analysis, Yamaguchi University for his technical assistance. This manuscript was improved by constructive comments from Tetsumaru Itaya of Japan Geochronology Network (NPO) and Kosuke Kimura of Osaka Metropolitan University. We also thank Koshi Yagi of Hiruzen Institute for Geology and Chronology Co., Ltd. for his editorial handling. This study was also supported by JSPS KAKENHI Grant Numbers 24540490, 15K05314 and 17H00834 to T.I.

References

Cangelosi, D., Broom-Fendley, S., Banks, D., Morgan, D. and Yardley, B. (2020) Light rare earth element redistribution during hydrothermal alteration at the Okorusu carbonatite complex, Namibia. *Mineralogical Magazine*, **84**, 49–64.

Dunkl, I., Mikes, T., Simon, K. and von Eynatten, H. (2008) Brief introduction to the Windows program Pepita: data visualization, and reduction, outlier rejection, calculation of trace element ratios and concentration from LA-ICP-MS data. *In* Sylvester, P. ed., *Laser Ablation ICP-MS in the Earth Sciences: Current practices and outstanding issues, Mineralogical Association of Canada Short Course Series*, **40**, 334–340.

Herzig, C.T., Kimbrough, D.L., Tainosho, Y., Kagami, H., Iizumi, S. and Hayasaka, Y. (1998) Late Cretaceous U/Pb zircon ages and Precambrian crustal inheritance in Ryoke granitoids, Kinki and Yanai districts, Japan. *Geochemical Journal*, **32**, 21–31.

Higashimoto, S., Nureki, T., Hara, I., Tsukuda, E. and Nakajima, T. (1983) *Geology of the Iwakuni district*. Quadrangle Series, Scale 1: 50,000, Geological Survey of Japan, 79p (in Japanese with English abstract).

Ikeda, Y. (2004) The Naganobori copper mine site. *In* Yamaguchi Prefecture ed., *The book of Yamaguchi Prefectural History, Archaeology*, **2**, 561–587 (in Japanese).

Ikeda, Y. (2015) Remains of the Naganobori copper mine: The oldest ancient copper mine in Nagato, Japan. *Nihon no Iseki*, **49**, Doseisha, Co., Ltd., Tokyo, 194p (in Japanese).

Imaoka, T. and Iizumi, S. (2009) Cretaceous–Paleogene igneous activity. *In:* Editorial Committee of Chugoku, Regional Geology of Japan ed., *Regional Geology of Japan, Volume 6: Chugoku district*, Asakura Publishing Co., Ltd., Tokyo, 247–339 (in Japanese).

Ishihara, S. (1977) The magnetite-series and ilmenite-series granitic rocks. *Mining Geology*, **27**, 293–305.

Ishihara, S. (1981) The granitoid series and mineralization. *Economic Geology 75th Anniversary Volume*, 458–484.

Ishihara, S., Sato, K. and Terashima, S. (1984) Chemical characteristics and genesis of mineralized, intermediate-series granitic pluton in the Hobenzan area, western Japan. *Mining Geology*, **34**, 401–418.

Japan Mining Industry Association (1965) *Overview of the Ore Deposits in Japan*. **1**, 297–298 (in Japanese).

Kato, T. (1916) The ore deposits in the environs of Hanano-yama, near the town of Oda, Province of Nagato, Japan. *Journal of Meiji College of Technology*, **1**, 1–95.

Kato, T. (1937) *New Geology of Ore Deposits*, revised edition. Fuzanbo Publishing Company, Tokyo, 757p (in Japanese).

Katsube, A., Hayasaka, Y., Sakaguchi, A. and Takahashi, Y. (2012) U–Pb zircon dating using Nd-YAG (213 nm) Laser ablation-ICP-MS, and evaluating the consistency with SHRIMP dating. *Journal of the Geological Society of Japan*, **118**, 762–767 (in Japanese with English abstract).

Kuno, Y. (1990) Consideration on the copper ingredient of the Todaiji Buddha Statue. *Studies of Archaeology, Proceedings of the Archaeological Institute of Kashihara*, **14**, 111–131 (in Japanese).

Ludwig, K.R. (2003) *Isoplot 3.00. A geochronological toolkit for Microsoft Excel*. Berkeley Geochronology Center Special Publication, no. 4, Berkeley, 70p.

Meinert, L.D. (1995) Compositional variation of igneous rocks associated with skarn deposits – Chemical evidence for a genetic connection between petrogenesis and mineralization. *In* Thompson, J.F.H., ed., *Magmas, fluids, and ore deposits, Mineralogical Association of Canada Short Course Series*, **23**, 401–418.

Meinert, L.D., Dipple, G.M. and Nicolescu, S. (2005) World skarn deposits. *In* Hedenquist, J.W., Thompson, J.F.H., Goldfarb, R.J. and Richards, J.P., eds., *Economic Geology 100th Anniversary Volume*, 299–336.

Nagashima, M., Akasaka, M. and Morifuku, Y. (2015) Ore and skarn mineralogy of the Yamato mine, Yamaguchi Prefecture, Japan, with emphasis on silver-, bismuth-, cobalt-, and tin-bearing sulfides. *Resource Geology*, **66**, 37–54.

Nagashima, M., Morishita, Y., Imoto, Y. and Imaoka, T. (2021) Ore and skarn mineralogy of the Eboshi deposit of the Naganobori copper mine, Yamaguchi, Japan. *Journal of Mineralogical and Petrological Sciences*, **116**, 26–44.

Nakajima, T., Takahashi, M., Imaoka, T. and Shimura, T. (2016) Chapter 4, Granitic Rocks. *In* Moreno, T., Wallis, S., Kojima, T. and Gibbons, W. eds., *The Geology of Japan*, The Geological Society of London, 251–272.

Nakamura, K. (1954) Cobalt ores, *In* Geological Survey of Japan ed., *Mineral Resources of Japan*, BI-c, 103–114 (in Japanese).

Nakano, T. and Ishihara, S. (2003) Geochemical characteristics of the Akiyoshi limestones, Japan and their bearing on exploration for blind skarn deposits. *Resource Geology*, **53**, 29–36.

Nambu, M., Tanida, K., Kitamura, T. and Sakurai, K. (1970) Heterogenite from Naganobori Mine, Yamaguchi Prefecture, Japan. *The Journal of the Japanese Association of Mineralogists, Petrologists and Economic Geologists*, **64**, 53–63 (in Japanese with English abstract).

Ogura, T. (1921) Investigation report of the Naganobori mine and Oda mine. *Report, Geological Survey of Japan*, **82**, 49–72 (in Japanese).

Ota, M. (1976) Geologic map of the Akiyoshi district. *Bulletin of the Akiyoshi-dai Museum of Natural History*, **12**, 1–34

Paces, J.B. and Miller, J.D.Jr. (1993) Precise U–Pb ages of Duluth Complex and related mafic intrusions, northeastern Minnesota: Geochronological insights to physical, petrogenetic, paleomagnetic, and tectonomagmatic processes associated with the 1.1 Ga Midcontinent Rift System. *Journal of Geophysical Research: Solid Earth*, **98**, 13997–14013.

Saito, T. (2001a) Comprehensive lead isotope analysis of Japanese coins issued in Nara to Yedo periods. *Bulletin of the National Museum of Japanese History*, **86**, 65–129 (in Japanese with English abstract).

Saito, T. (2001b) Lead isotope analysis of tricolored glaze in Nara period and green glaze in Heian period. *Bulletin of the National Museum of Japanese History*, **86**, 199–208 (in Japanese with English abstract).

Sano, S., Hayasaka, Y. and Tazaki, K. (2000) Geochemical characteristics of Carboniferous greenstones in the Inner Zone of Southwest Japan. *Island Arc*, **9**, 81–96.

Sasaki, Y., Imaoka, T., Nagashima, M., Nakashima, K., Sonehara, T., Yagi, K. and Itaya, T. (2016) The Cretaceous Ofuku pluton and its relation to mineralization in the western Akiyoshi Plateau, Yamaguchi Prefecture, Japan. *Resource Geology*, **66**, 85–113.

Sasaki, Y., Imaoka, T., Nakashima, K. and Fujikawa, M. (2014) Geochemical characteristics and fluid inclusions of intrusive rocks in the Akiyoshi Limestone, and their bearing on mineralization. *Bulletin of the Akiyoshi-dai Museum of Natural History*, **49**, 7–23 (in Japanese with English abstract).

Shibata, K. and Ishihara, S. (1974) K–Ar ages of the major tungsten and molybdenum deposits in Japan. *Economic Geology*, **69**, 1207–1214.

Smith, M. P. and Henderson, P. (2000) Preliminary fluid inclusion constraints on fluid evolution in the Bayan Obo Fe–REE–Nb deposit, Inner Mongolia, China. *Economic Geology*, **95**, 1371–1388.

Takahashi, T. (2001a) A study on the mintage and the supply of its raw materials in Japan. *Bulletin of the National Museum of Japanese History*, **86**, 131–184 (in Japanese with English abstract).

Takahashi, T. (2001b) A study of tricolored glaze and green glaze from a viewpoint of scientific research. *Bulletin of the National Museum of Japanese History*, **86**, 209–232 (in Japanese with English abstract).

Tatsumi, Y., Kani, T., Ishizuka, H., Maruyama, S. and Nishimura, Y. (2000) Activation of Pacific mantle plumes during the Carboniferous: Evidence from accretionary complexes in southwest Japan. *Geology*, **28**, 580–582.

Ueda, K. (2002) Copper production at Naganobori mine for Nara Buddha construction in the first half of 8th century and its development afterwards. *Fifth International Conference on the Beginnings of the Use of Metals and Alloys, Gyeongju, Korea*, 19–27.

Verplanck, P.L. (2017) The role of fluids in the formation of rare earth element deposits. *Procedia Earth and Planetary Science*, **17**, 758–761.

Watanabe, M. (2009) Naganobori mine. *In* Editorial Committee of Chugoku, Regional Geology of Japan ed., *Regional Geology of Japan, Volume 6: Chugoku district*, Asakura Publishing Co., Ltd., Tokyo, 453–454 (in Japanese).

Watanabe, M., Nishido, H., Moriwaki, H., Higashimoto, S. and Kubota, Y. (1988) K–Ar ages of skarn deposits in the Inner Zone of southwestern Japan. *Geochemical Journal*, **22**, 231–236.

Whitney, D.L. and Evans, B.W. (2010) Abbreviations for names of rock-forming minerals. *American Mineralogist*, **95**, 185–187.

Williams-Jones, A.E. and Migdisov, A.A. (2014) Experimental constraints on the transport and deposition of metals in ore-forming hydrothermal systems. *Society of Economic Geologists, Special Publication*, **18**, 77–95.

Williams-Jones, A. E., Migdisov, A. A. and Samson, I. M. (2012) Hydrothermal mobilisation of the rare earth elements—a tale of “Ceria” and “Yttria”. *Elements*, **8**, 355–360.

Wyllie, P.J., Cox, K.G. and Biggar, G.M. (1962) The habit of

apatite in synthetic systems and igneous rocks. *Journal of Petrology*, **3**, 238–243.

Yoshikawa, R., Motomura, Y., Nakanishi, T. and Izawa, E. (2005) Ores and smelting slag of the Ancient Naganobori Copper mine. *Journal of the Historical Study Group of Mining and Metallurgy, Japan*, **50**, 27–40 (in Japanese).

Yoshimura, K., Kurisaki, K., Okamoto, T., Fujikawa, M., Ikeda, Y., Yamada, T. and Matsuda, H. (2014) Sulfide ore smelting at the Naganobori copper mine recorded on speleothems from the Ogiri no. 4 pit on the Akiyoshi-dai Plateau, Yamaguchi, Japan. *ISIJ International*, **54**, 1147–1154.

地質技術 第 12 号，5-17 頁（2022）

山口県長登鉱山の鉱化作用に関係した花の山プルトンの U–Pb ジルコン年代

今岡照喜 [1)]・早坂康隆 [2)]・永嶌真理子 [1)]・曽根原崇文 [3)]・宮内真奈 [4)]

[1)] 山口大学大学院創成科学研究科，〒 753-8512　山口県山口市吉田 1677-1
[2)] 広島大学理学部地球惑星システム学科，〒 739-8526　広島県東広島市鏡山 1-3-1
[3)] 株式会社 蒜山地質年代学研究所，〒 703-8252　岡山市中区中島 2-5
[4)] 古賀市役所，〒 811-3192　福岡県古賀市駅東 1-1-1

日本語要旨　山口県秋吉台東部に位置する長登鉱山は古代に銅を採掘し，皇朝十二銭の鋳造など国家的事業に使われたことで知られる．長登鉱山の鉱化作用と白亜紀の花の山花崗斑岩のマグマ活動の関係を明らかにする目的で後者の岩石記載およびU–Pb年代測定を行った．構成鉱物の化学組成を分析したところ，フッ素に富む黒雲母(～0.58 wt.%)，チタン石(～4.42 wt.%)，フッ素燐灰石(～4.11 wt.%)，モナズ石–(Ce)(～0.67 wt.%)，褐簾石–(Ce) (～0.40 wt.%)が見出された．これらの鉱物は希土類元素(REE)にも富んでおりフッ素とREEは花の山プルトンの残液に濃集したことを示す．花の山花崗斑岩のマグマ性ジルコンについて101.5 ± 0.7 Maの$^{206}Pb/^{238}U$年代が得られた．これは山口県の山陽帯におけるイルメナイト系列の花崗岩に伴われるタングステン鉱床区の年代を示している．

付録：鉱山名等日本語対応

Abu Group　阿武層群
Akaono silver copper mine　赤小野銀銅山
Akiyoshi　秋吉
Akiyoshi Limestone Group　秋吉石灰岩層群
Akiyoshi Plateau　秋吉台
Beppu　別府
Eboshi deposit　烏帽子鉱床
Fujigatani mine　藤ヶ谷鉱山
Hakushiki deposit　箔鋪鉱床
Hanano-yama granite porphyry　花の山花崗斑岩
Hanano-yama pluton　花の山プルトン
Imori deposit　伊森鉱床
Kaerimizu　帰り水
Kanmon Group　関門層群
Kitabira mine　北平鉱山
Kiwada mine　喜和田鉱山
Kuga mine　玖珂鉱山
Kyozuka-yama　経塚山
Mine Group　美祢層群
Naganobori deposit　長登鉱床
Naganobori mine　長登鉱山
Nakamura　中村
Oda　大田（地名）
Oda deposit　大田鉱床
Ofuku pluton　於福プルトン
Ogiri deposit　大切鉱床
Ota Group　大田層群
Sanjo mine　三条鉱山
Tsunemori Formation　常森層
Ueyama　植山
Umegakubo deposit　梅ケ窪鉱床
Yamato mine　大和鉱山